SCIENTIFIC REPORTS

OPEN

Galvanomagnetic properties of the putative type-II Dirac semimetal $PtTe_2$

Received: 23 May 2018
Accepted: 9 July 2018
Published online: 26 July 2018

Orest Pavlosiuk[1] & Dariusz Kaczorowski[2]

Platinum ditelluride has recently been characterized, based on angle-resolved photoemission spectroscopy data and electronic band structure calculations, as a possible representative of type-II Dirac semimetals. Here, we report on the magnetotransport behavior (electrical resistivity, Hall effect) in this compound, investigated on high-quality single-crystalline specimens. The magnetoresistance (MR) of $PtTe_2$ is large (over 3000% at $T = 1.8$ K in $B = 9$ T) and unsaturated in strong fields in the entire temperature range studied. The MR isotherms obey a Kohler's type scaling with the exponent $m = 1.69$, different from the case of ideal electron-hole compensation. In applied magnetic fields, the resistivity shows a low-temperature plateau, characteristic of topological semimetals. In strong fields, well-resolved Shubnikov – de Haas (SdH) oscillations with two principle frequencies were found, and their analysis yielded charge mobilities of the order of 10^3 cm^{2}V^{-1}s^{-1} and rather small effective masses of charge carriers, 0.11 m_e and 0.21 m_e. However, the extracted Berry phases point to trivial character of the electronic bands involved in the SdH oscillations. The Hall effect data corroborated a multi-band character of the electrical conductivity in $PtTe_2$, with moderate charge compensation.

Topological semimetals (TSs) form an outstanding group of materials characterized by perfect linear dispersion of some bulk electronic states[1,2]. In accordance with presence or absence of Lorentz invariance, one discriminates type-I and type-II systems[3]. In the latter class of TSs, Dirac cone is strongly tilted with respect to Fermi level[4]. Both type-I and type-II TSs can be composed from Dirac or Weyl fermions, depending on what kind of symmetries is preserved[5]. Nontrivial electronic structures of TSs give rise to unusual electronic transport properties, commonly considered being highly prospective for various electronic devices of new kind. A hallmark feature of TSs is chiral magnetic anomaly (CMA), which manifests itself as a negative magnetoresistance (MR) observed when electric and magnetic fields are collinear[6]. Actually, negative MR was found in many TSs, more often in type-I materials[7–11] but also in a few type-II systems[12]. Another smoking-gun signature of TSs is the existence of topological surface states, which have a form of Fermi-arcs[1,2]. Their presence was confirmed experimentally in a large number of TSs, among them Cd_3As_2[13], $MoTe_2$[14], WTe_2[15] and TaAs[16].

Type-II topological semimetallic states have been revealed in several transition metal dichalcogenides and in MA_3 (M = V, Nb, Ta; A = Al, Ga, In) icosagenides[3,4,14,17–20]. Within the former group of compounds, $MoTe_2$ and WTe_2 have been classified as type-II Weyl semimetals[14,21], whereas platinum and palladium dichalcogenides have been established via angle-resolved photoemission spectroscopy (ARPES) experiments to represent the family of type-II Dirac semimetals[3,18,22]. The TSs nature of $PdTe_2$ is reflected in its peculiar magnetotransport behavior[23,24]. In turn, no comprehensive study on the electronic transport properties of the Pt-bearing counterpart has been reported in the literature up to date. In this work, we investigated the galvanomagnetic properties of $PtTe_2$ with the main aim to discern features appearing due to the alleged nontrivial topology of its electronic band structure.

Results and Discussion

Electrical resistivity, magnetic field-induced plateau and magnetoresistance. Figure 1a shows the results of electrical resistivity, ρ, measurements performed on single-crystalline sample of $PtTe_2$, as a function of temperature, T, with electric current, i, flowing within the hexagonal $a - b$ plane. The overall behavior of $\rho(T)$ indicates a metallic character of the compound. The resistivity decreases from the value of 24.09 $\mu\Omega$ cm at

[1]Institute of Low Temperature and Structure Research, Polish Academy of Sciences, P. O. Box 1410, 50-950 Wrocław, Poland. [2]Institute of Molecular Physics, Polish Academy of Sciences, Mariana Smoluchowskiego 17, 60-179, Poznań, Poland. Correspondence and requests for materials should be addressed to D.K. (email: d.kaczorowski@int.pan.wroc.pl)

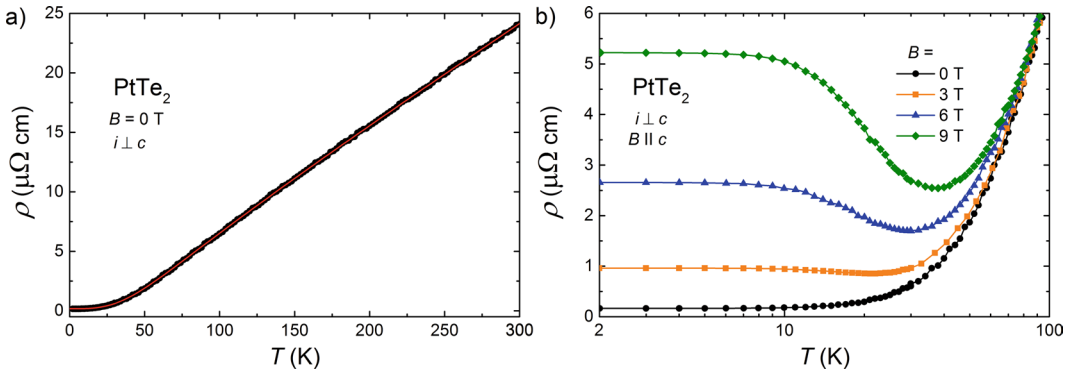

Figure 1. Electrical resistivity of $PtTe_2$. (**a**) Temperature dependence of the electrical resistivity measured in zero magnetic field with electric current i confined within the $a-b$ plane of the crystallographic unit cell. Solid red curve represents the result of fitting the BG law to the experimental data. (**b**) Low-temperature resistivity ($i \perp c$) measured as a function of temperature in transverse magnetic field ($B \parallel c$).

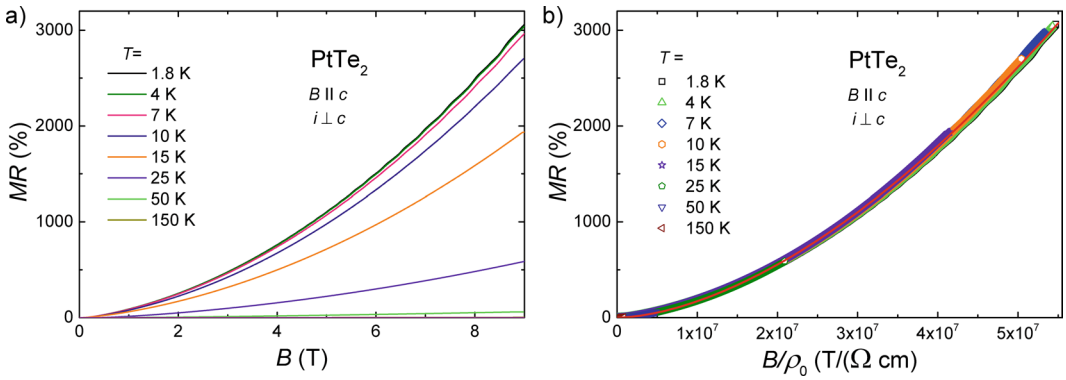

Figure 2. Magnetotransport properties of $PtTe_2$. (**a**) Magnetoresistance measured with $i \perp c$ and $B \parallel c$ at several constant temperatures. (**b**) Kohler's plot of the magnetoresistance data. Red solid line is the result of fitting the Kohler's equation to the experimental data.

$T = 300$ K to 0.17 $\mu\Omega$ cm at $T = 2$ K, yielding the residual resistivity ratio RRR $= \rho(300\text{K})/\rho(2\text{K})$ equal to 142. The magnitudes of both $\rho(2\text{K})$ and RRR indicate high crystallinity of the specimen measured (RRR is approximately 5 times larger than that reported for $PtTe_2$ in ref.[18]). As displayed in Fig. 1a (note the red solid line), in the whole temperature range covered, $\rho(T)$ can be very well approximated with the Bloch-Grüneisen (BG) law:

$$\rho(T) = \rho_0 + A\left(\frac{T}{\Theta_D}\right)^k \int_0^{\frac{\Theta_D}{T}} \frac{x^k}{(e^x - 1)(1 - e^{-x})} dx, \tag{1}$$

where ρ_0 is the residual resistivity, accounting for scattering conduction electrons on crystal imperfections, while the second term represents electron-phonon scattering (Θ_D stands for the Debye temperature). The least-squares fitting yielded the parameters: $\rho_0 = 0.17\ \mu\Omega$ cm, $\Theta_D = 253$ K, $A = 11.6\ \mu\Omega$ cm and $k = 3.23$. The value of k is smaller than $k = 5$, expected for simple metals, yet similar to k exponents determined for several monopnictides[25–27].

The temperature dependencies of the electrical resistivity of $PtTe_2$ measured in transverse magnetic field ($i \perp c$ axis and $B \parallel c$ axis) are gathered in Fig. 1b. In non-zero B, $\rho(T)$ is a non-monotonous function of temperature, showing an upturn below a certain slightly field-dependent temperature T^*, and then forming a plateau at the lowest temperatures. With increasing magnetic field, the magnitude of the resistivity in the turn-on and plateau regions distinctly increases. Similar behavior was considered as a fingerprint of the presence of nontrivial topology in the electronic structure of several TSs[28–31]. Another possible explanation of this type of magnetic field governed changes in $\rho(T)$ is a metal-insulator transition[29,32,33]. However, as discussed first for WTe_2[34], and afterwards, e.g., for rare-earth monopnictides[25–27,35–41], the magnetic field induced upturn in $\rho(T)$ may appear also in trivial semimetals, which are close to perfect charge carriers compensation. We presume that the latter mechanism is also fully appropriate for the electrical transport behavior in $PtTe_2$.

In order to examine the actual nature of the galvanomagnetic behavior observed for $PtTe_2$, transverse magnetoresistance, MR $= [\rho(B) - \rho(B = 0)]/\rho(B = 0)$, measurements were performed at several constant temperatures in the configuration $i \perp c$ axis and $B \parallel c$ axis. As can be inferred from Fig. 2a, in $B = 9$ T, MR taken at $T = 1.8$ K achieves a giant value of 3060%, which is an order of magnitude larger than MR determined in the same conditions for the related system $PdTe_2$[23], and almost equal to that reported for the type-II Weyl semimetal $MoTe_2$[42].

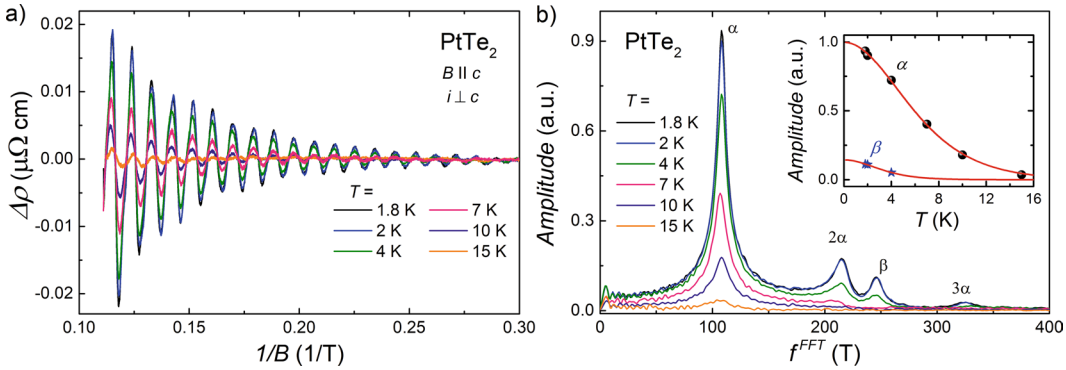

Figure 3. Shubnikov-de Haas effect in $PtTe_2$. (**a**) Oscillating part of the electrical resistivity measured at several different temperatures with $i \perp c$ axis and $B \parallel c$ axis, plotted as a function of inverse magnetic field. (**b**) Fast Fourier transform spectrum obtained from the analysis of the data presented in panel (a). Inset shows the temperature dependencies of the amplitudes of two principal frequencies in the FFT spectra. Solid lines represent the fits of Eq. 2 to the experimental data.

With increasing temperature, MR measured in $B = 9$ T does not change significantly up to about 10 K (i.e., in the plateau region of $\rho(T)$), and then decreases rapidly. However, even at $T = 150$ K, MR remains exceptionally large exceeding 500% in 9 T. At each of the temperatures studied, MR shows no tendency towards saturation in strong fields. MR behavior similar to that of $PtTe_2$ was established before for several TSs[23,28,30,42–44]. However, unsaturated MR can be also attributed to perfect or almost perfect carrier compensation in a semimetallic material[45].

Remarkably, as demonstrated in Fig. 2b, the MR isotherms of $PtTe_2$ obey the Kohler's rule in the entire temperature range studied. This finding rules out the scenario of metal-insulator transition as a possible mechanism of the magnetic field driven changes in the electrical transport of $PtTe_2$. The MR data collapse onto a single curve, which can be approximated by the expression: $MR \propto (B/\rho_0)^m$, with the exponent $m = 1.69$ (note the red solid line in Fig. 2b). While $m = 2$ is expected for materials with perfect electron-hole balance, and the obtained value is also smaller than $m = 1.92$ reported for WTe_2[34], it is similar to those found for some monopnictides, which were reported as trivial semimetals fairly close to charge compensation[26,37,40].

Quantum oscillations. In order to characterize the Fermi surface in $PtTe_2$, we investigated quantum oscillations in $\rho(B)$ (Shubnikov–de Haas effect) at a few different temperatures. Figure 3a shows the oscillatory part of the electrical resistivity, $\Delta\rho$, obtained by subtraction of the second-order polynomial from the experimental data, plotted as a function of reciprocal magnetic field, $1/B$. As can be inferred from this figure, the SdH oscillations remain discernible at temperatures up to at least 15 K, however, their amplitudes systematically decrease with increasing temperature. Fast Fourier transform (FFT) analysis, the results of which are presented in Fig. 3b, disclose four features at the oscillations frequencies f_i^{FFT} (i represents the Fermi surface pocket label). The most prominent peak occurs at $f_\alpha^{FFT} = 108$ T, and the corresponding Fermi surface pocket will be labeled thereinafter as α. The next feature occurs at $f_{2\alpha}^{FFT} = 215$ T and it is the second harmonic frequency of f_α^{FFT}. Then, the peak with its maximum at $f_\beta^{FFT} = 246$ T can be attributed to another Fermi surface pocket, labeled β in what follows. Eventually, the very weak maximum centered at $f_{3\alpha}^{FFT} = 325$ T likely arises as the third harmonics of f_α^{FFT}. It is worthwhile noting that the FFT spectrum of $PtTe_2$ is very similar to that reported for $PdTe_2$ in ref.[23] but differs from the FFT data shown for the same compound in ref.[24]. Using the Onsager relation $f_i^{FFT} = hS/e$, where S stands for the area of Fermi surface cross-section, one finds for the two pockets in $PtTe_2$ the values $S_\alpha = 1.03 \times 10^{-2}$ Å^{-2} and $S_\beta = 2.34 \times 10^{-2}$ Å^{-2}. Assuming circular cross-sections, the corresponding Fermi wave vectors are $k_{F,\alpha} = 5.73 \times 10^{-2}$ Å^{-1} and $k_{F,\beta} = 8.63 \times 10^{-2}$ Å^{-1}. Then, if we assume that both Fermi surface pockets are spherical, which is poor approximation, the carrier densities in these two pockets would be equal to $n_\alpha = 6.35 \times 10^{18}$ cm^{-3} and $n_\beta = 2.17 \times 10^{19}$ cm^{-3}.

The electronic structure calculated for $PtTe_2$[3,18] comprises three bands crossing the Fermi level, one hole-like band, located at the center of the Brillouin zone, and two electron-like bands. The fact that we observed experimentally only two principle frequencies is probably due to very small size of the third Fermi surface pocket or might arise owing to somewhat lower position of the Fermi level in the single crystal studied. From the comparison of the values of $k_{F,i}$ obtained from the FFT analysis and sizes of the calculated electronic bands[3], one may presume that the α Fermi surface pocket corresponds to one of the electron-like bands and the β Fermi surface pocket represents the hole-like band.

The inset to Fig. 3b displays the temperature variations of the FFT amplitudes, $R_i(T)$, corresponding to the α and β Fermi surface pockets in $PtTe_2$. The gradual damping of both oscillations with rising temperature can be described by formula[46]:

$$R_i(T) \propto (\lambda m_i^* T/B_{eff})/\sinh(\lambda m_i^* T/B_{eff}), \quad (2)$$

where m_i^* is the effective cyclotron mass of charge carriers, $B_{eff} = 4.5$ T was calculated as $B_{eff} = 2/(1/B_1 + 1/B_2)$ ($B_1 = 3$ T and $B_2 = 9$ T are the borders of the magnetic field window in which the FFT analysis was performed),

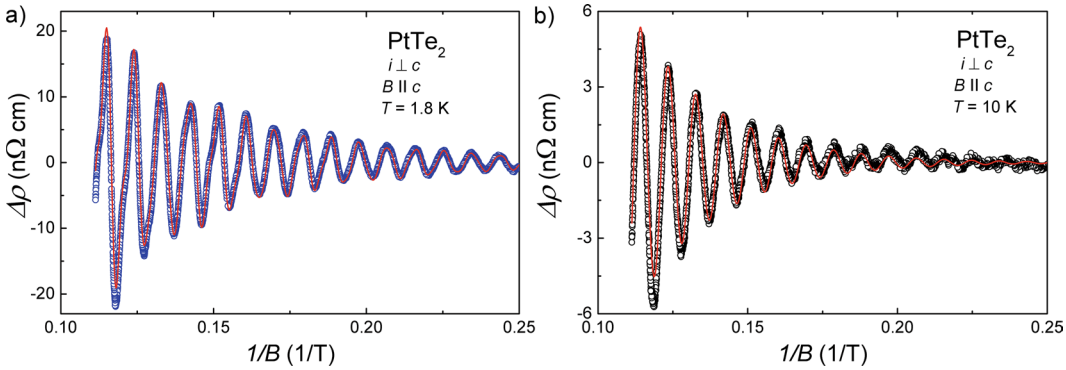

Figure 4. Lifshitz-Kosevich analysis of the magnetotransport in $PtTe_2$. Oscillating part of the electrical resistivity measured at (**a**) $T = 1.8$ K and (**b**) $T = 10$ K, plotted as a function of inverse magnetic field. Solid red lines correspond to the results of fitting Eq. 3 to the experimental data.

and $\lambda = 14.7$ T/K was obtained from the relationship $\lambda = 2\pi^2 k_B m_e / e\hbar$ (m_e stands for the free electron mass, and k_B is the Boltzmann constant). The fitting shown in the inset to Fig. 3b yielded $m_\alpha^* = 0.11 m_e$ and $m_\beta^* = 0.21 m_e$. It is worth noting that the effective mass determined for the α Fermi surface pocket in $PtTe_2$ is almost equal to that reported for the Pd-bearing counterpart[23].

In the next step, we attempted to determine the phase shift, φ_i, in the SdH oscillations, which is directly related to the Berry phase, $\varphi_{B,i}$, of the carries involved. There are known a few methods of extracting φ_i, and the proper interpretation of their values remains debatable[47–50]. The most reliable approach is direct fitting to the experimental data of the Lifshitz-Kosevich (LK) function[46]:

$$\Delta\rho \propto \frac{1}{\sqrt{B}} \sum_i \frac{p_i \lambda m_i^* T/B}{\sinh(p_i \lambda m_i^* T/B)} \exp(-p_i \lambda m_i^* T_{D,i}/B) \cos(2\pi(p_i f_i/B + \varphi_i)), \tag{3}$$

where p_i is the harmonic number, f_i is the oscillation frequency, and $T_{D,i}$ stands for the Dingle temperature. In Fig. 4a, there is shown the result of fitting the LK function to the oscillating resistivity of $PtTe_2$ observed at $T = 1.8$ K (note the red solid line). As discussed above, at this temperature, the FFT spectrum comprises three peaks, and thus the sum in Eq. 3 consists of as many as three contributions. In order to reduce the total number of free parameters in this equation, the effective masses were fixed at the values obtained from Eq. 2 (see above). With this simplification, one obtained the parameters: $f_\alpha = 108.1$ T, $T_{D,\alpha} = 9.1$ K and $\varphi_\alpha = 0.65$ for the α band, and $f_\beta = 246$ T, $T_{D,\beta} = 5$ K and $\varphi_\beta = 0.54$ for the β band. Remarkably, the so-obtained values of f_i are almost identical to those derived from the afore-described FFT analysis, hence confirming the internal consistency of the approach applied. Using the Dingle temperatures, the quantum relaxation time, $\tau_{q,i}$, could be calculated from the relation $\tau_{q,i} = \hbar/(2\pi k_B T_{D,i})$ to be equal to 1.34×10^{-13} s and 2.43×10^{-13} s for the α and β bands, respectively. Then, the quantum mobility of charge carriers, $\mu_{q,i}$, were estimated from the relationship $\mu_{q,i} = e\tau_{q,i}/m_i^*$ to be 2138 $cm^2 V^{-1} s^{-1}$ and 2038 $cm^2 V^{-1} s^{-1}$ for the α and β bands, respectively.

The phase shift φ_i in Eq. 3 is generally a sum $\varphi_i = -1/2 + \varphi_{B,i} + \delta_i$, where δ_i represents the dimension-dependent correction to the phase shift[49]. In two-dimensional (2D) case, this parameter amounts zero, while in three-dimensional (3D) case δ_i is equal to $\pm 1/8$, and its sign depends on type of charge carriers and kind of cross-section extremum. Supposing that the SdH oscillations in $PtTe_2$ originate from 3D bands with carriers moving on their maximal orbits, one can set $\delta = -1/8$ for electrons and $\delta = 1/8$ for holes. With this assumption, the Berry phases $\varphi_{B,\alpha} = 0.55\pi$ and $\varphi_{B,\beta} = 1.83\pi$ were obtained for the α and β bands, respectively.

To check the reliability of the LK analysis performed, Eq. 3 was also used to describe the experimental data measured at $T = 10$ K. At this temperature, just one peak in the FFT spectrum is discernible (see Fig. 3b), which corresponds to the α Fermi surface pocket. The result of fitting the LK formula is presented in Fig. 4b (note the red solid line), and the so-derived values of the parameters are: $f_\alpha = 108.1$ T, $T_{D,\alpha} = 12.6$ K and $\varphi_{B,\alpha} = 0.46\pi$. Notably, the agreement between the f_α values obtained at $T = 10$ K and $T = 1.8$ K is perfect. The value of $T_{D,\alpha}$ implies $\mu_q = 1544$ $cm^2 V^{-1} s^{-1}$. Clearly, with increasing temperature, the Dingle temperature increases and consequently the quantum charge carriers mobility becomes smaller, which is probably due to increasing the scattering rate. In turn, the Berry phase of the α band was found almost independent of temperature. All the parameters obtained from the LK approach to the magnetotransport in $PtTe_2$ are gathered in Table 1.

Another commonly applied technique for Berry phase derivation is using Landau level (LL) fan diagrams. Though in case of multi-frequency oscillations this method is obstructed by possible superposition of the quantum oscillation peaks that hinders precise determination of the Landau level index for a given frequency[51], we made an attempt to construct the LL fan diagram for the α Fermi pocket in $PtTe_2$. As it is apparent from Fig. 3b, the FFT maximum occurring at $f_\alpha^{FFT} = 108$ T is fairly well separated from the other FFT peaks, and hence one could filter this oscillation with reasonably high accuracy. For $PtTe_2$ one finds $\rho > \rho_{xy}$ (ρ_{xy} is the Hall resistivity discussed in the next section), and therefore the maxima in the oscillatory resistivity measured at $T = 1.8$ K (see Fig. 4a) were numbered by integers, n, and the minima by half-integers, $n + 1/2$. The result of this approach is shown in the main panel of Fig. 5. A linear fit of the LL indices (note the solid line) gives an intercept of 0.62,

T (K)	band	f_i^{FFT} (T)	f_i (T)	m^* (m_e)	T_D (K)	τ_q (s)	μ_q ($cm^2V^{-1}s^{-1}$)	φ_B
1.8	α	108	108.1	0.11	9.1	1.34×10^{-13}	2138	0.55π
	β	246	246	0.21	5	2.43×10^{-13}	2038	1.83π
10	α	108	108.5	0.11	12.6	9.65×10^{-14}	1544	0.46π

Table 1. Parameters extracted from the LK analysis of the SdH oscillations in $PtTe_2$. T - temperature; f_i^{FFT} - oscillation frequency obtained from the FFT analysis; f_i - oscillation frequency obtained from Eq. 3; m^* - effective mass; T_D - Dingle temperature; τ_q - quantum relaxation time; μ_q - quantum mobility; φ_B - Berry phase.

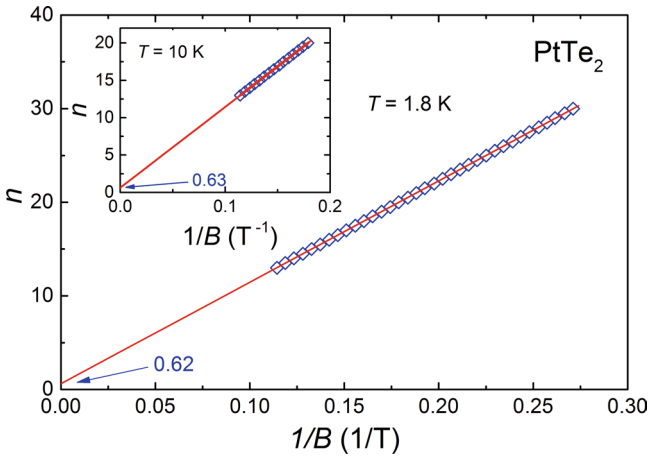

Figure 5. Landau level fan diagrams for $PtTe_2$. The Landau level indices, n, determined for the α Fermi surface pocket at $T = 1.8$ K plotted as a function of inverse magnetic field. Inset shows the LL plot of the SdH oscillations measured at $T = 10$ K. Solid lines represent the linear fits to the LL data.

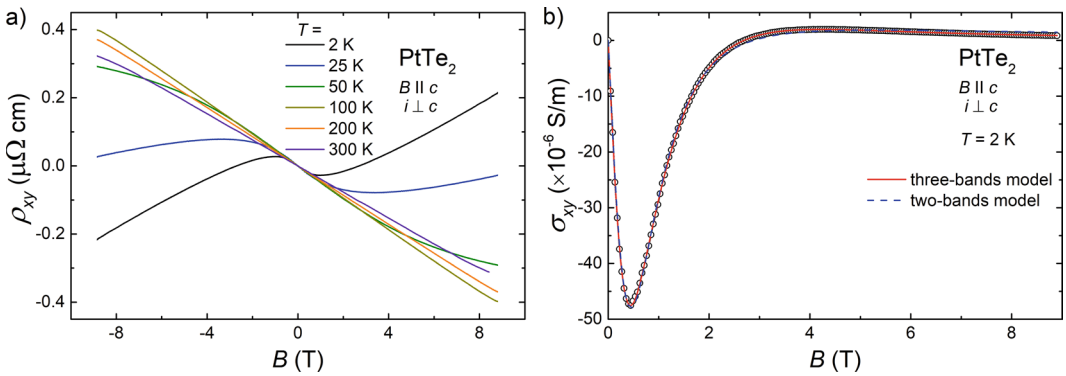

Figure 6. Hall effect in $PtTe_2$. (**a**) Magnetic field dependencies of the Hall resistivity measured at several different temperatures with $i \perp c$ axis and $B \parallel c$ axis. (**b**) Hall conductivity as a function of magnetic field at $T = 2$ K. Blue dashed line represents the fit with two-bands model, and red solid line stands for result obtained with three-bands model.

which corresponds to the Berry phase $\varphi_{B,\alpha} = 0.51\pi$. In turn, the slope of this straight line defines the oscillation frequency $f_\alpha = 108.3$ T.

At $T = 10$ K, the electrical resistivity of $PtTe_2$ oscillates in the transverse magnetic field with only one frequency (cf. Fig. 3b), so building the LL fan diagram is straightforward. As can be inferred from the inset to Fig. 5, the LL indices plot yields the intercept 0.63, which is almost the same as that obtained at the lower temperature. Also, the slope of the straight line ($f_\alpha = 108.3$ T) is identical with that determined at 1.8 K, and furthermore it is very close to the FFT value (see Table 1). Most importantly, all the parameters extracted from the LL indices plots are in perfect agreement with the quantities obtained for the α Fermi pocket from the LK analysis, which unambiguously corroborates the correctness of both techniques applied for $PtTe_2$.

Model	n_h (cm^{-3})	μ_h ($cm^2V^{-1}s^{-1}$)	n_{e1} (cm^{-3})	μ_{e1} ($cm^2V^{-1}s^{-1}$)	n_{e2} (cm^{-3})	μ_{e2} ($cm^2V^{-1}s^{-1}$)
two-bands	5.99×10^{20}	7179	5.05×10^{20}	17373	—	—
three-bands	7.91×10^{20}	4740	3.8×10^{20}	19240	3.82×10^{20}	2564

Table 2. Parameters obtained for $PtTe_2$ from multi-bands models analyses of the the Hall effect data. n_h - hole concentration; μ_h - hole mobility; n_{e1} and n_{e2} - electron concentrations; μ_{e1} and μ_{e2} - electron mobilities.

Hall effect. The results of Hall resistivity measurements, performed on single-crystalline $PtTe_2$ with electric current flowing within the basal plane of the hexagonal unit cell and magnetic field applied along the *c* axis, are shown in Fig. 6a. At $T = 2$ K, $\rho_{xy}(B)$ behaves in a rather complex manner. In weak magnetic fields, it is negative and exhibits a shallow minimum. Near 2 T, the Hall resistivity changes sign to positive, and then its magnitude increases with increasing *B*. The $\rho_{xy}(B)$ isotherm measured at 25 K shows a fairly similar field variation, yet the positive contribution in strong fields remains too small to cause sign reversal. At higher temperatures, one observes a gradual straightening of the $\rho_{xy}(B)$ with rising *T*. The overall behavior of the Hall effect in $PtTe_2$ confirms the multi-band character of the electrical transport in this material. It is worth recalling that very similar Hall response was observed for the closely related compound $PdTe_2$[24].

For quantitative analysis of the experimental data, first a two-bands Drude model was applied. For this purpose, $\rho_{xy}(B)$ measured at $T = 2$ K was converted to the Hall conductivity $\sigma_{xy} = \rho_{xy}/(\rho_{xy}^2 + \rho^2)$, as displayed in Fig. 6b. Next, $\sigma_{xy}(B)$ was fitted by the formula:

$$\sigma_{xy}(B) = eB\left(\frac{n_h\mu_h^2}{1 + (\mu_h B)^2} + \frac{n_{e1}\mu_{e1}^2}{1 + (\mu_{e1}B)^2}\right), \tag{4}$$

where n_{e1} and μ_{e1}, n_h and μ_h stand for the carrier concentrations and the carrier mobilities of electron- and hole-like bands, respectively. As can be inferred from Fig. 6b, the so-obtained approximation of the measured $\sigma_{xy}(B)$ data (note the blue dashed line) is not ideal. An obvious reason for the discrepancy between the experiment and the two-band model could be contribution from another band, the presence of which was revealed in the ab-initio calculations of the electronic structure of $PtTe_2$[3,18].

Therefore, in the next step, the Hall conductivity was analysed in terms of a three-bands model:

$$\sigma_{xy}(B) = eB\left(\frac{n_h\mu_h^2}{1 + (\mu_h B)^2} + \frac{n_{e1}\mu_{e1}^2}{1 + (\mu_{e1}B)^2} + \frac{n_{e2}\mu_{e2}^2}{1 + (\mu_{e2}B)^2}\right). \tag{5}$$

where n_{e2} and μ_{e2} account for the carrier concentration and the carrier mobility, respectively, of another electron-like band in $PtBi_2$. The result of fitting Eq. 5 to the experimental $\sigma_{xy}(B)$ data is shown as red solid line in Fig. 6b. Clearly, the obtained description is much better than that with the two-bands model.

The fitting parameters derived in the two approaches are listed in Table 2. Both models yielded large carriers concentrations of the order of 10^{20} cm^{-3}. It is worth noting that very similar charge densities were found in the Dirac semimetal $PtBi_2$[52]. On the contrary, for the type-II Weyl semimetal WTe_2 the carrier concentrations were reported to be up to two orders of magnitude larger than those in $PtTe_2$[53]. As regards the level of carrier compensation, the two-bands model yielded considerable charge imbalance given by the ratio $n_h/n_{e1} = 1.19$, however the three-bands model led to fairly balanced scenario $n_h/(n_{e1} + n_{e2}) = 1.04$. Recently, similar degree of electron-hole compensation was established, e.g., in semimetallic monobismuthides YBi and LuBi[27]. The mobilities of charge carriers in $PtTe_2$ were found very high, especially that obtained for one of the electron-like Fermi surface pockets ($\mu_{e1} \sim 2 \times 10^4$ $cm^2V^{-1}s^{-1}$). Though the latter value is not such large as the carriers mobilities in Cd_3As_2[54] or NbP[28] it exceeds the values reported for type-II Weyl semimetals $MoTe_2$[42], WTe_2[55], and WP_2[53]. It is worth noting that the carriers mobility derived from the Hall effect data are larger than the quantum mobilities determined in the analyses of the SdH oscillations. Similar finding was reported for other TSs, like Cd_3As_2[54], ZrSiS[56], WP_2[43], and $PtBi_2$[52]. The discrepancy likely arises due to the fact that the quantum mobility is affected by all possible scattering processes, whereas the Hall mobility is sensitive to small-angle scattering only[46].

Angle-dependent magnetoresistance. In order to check whether $PtTe_2$ demonstrates CMA, angle-dependent magnetotransport measurements were performed at $T = 2$ K. In these experiments, electric current was always flowing within the hexagonal $a - b$ plane, while the angle θ between current and magnetic field direction was varied from $\theta = 90°$ ($B \perp i$) to $\theta = 0°$ ($B \parallel i$). As can be inferred from Fig. 7, the electrical resistivity rapidly decreases on deviating from the transverse configuration, and eventually for the longitudinal geometry ρ measured in $B = 9$ T is about an order of magnitude smaller than that for $B \perp i$.

Clearly, the longitudinal MR experiments did not provide any evidence for CMA in $PtTe_2$. A possible source for that may be large contribution of non-Dirac states to the measured resistivity. At odds with the Drude theory, which predicts zero MR for $B \parallel i$[57], in several materials sizeable positive longitudinal MR was observed. Among the theories which interpret this phenomenon[58–61], that accounting for Fermi surface anisotropy[61] seems appropriate for $PtTe_2$. Within the latter approach, positive longitudinal MR up to ~100% can be expected for strongly anisotropic systems. In consequence, CMA would be discernible only if its negative contribution to the longitudinal MR is larger than the positive term due to trivial electronic bands.

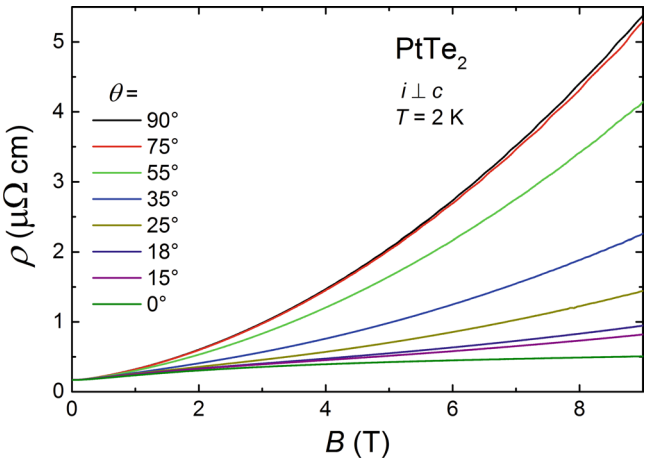

Figure 7. Angle-dependent magnetotransport in $PtTe_2$. Magnetic field dependencies of the electrical resistivity measured at $T = 2$ K with $i \perp c$ axis and external magnetic field oriented at several different angles in relation to the electric current direction.

Conclusions

Our comprehensive investigations of the galvanomagnetic properties of the alleged type-II Dirac semimetal $PtTe_2$, performed on high-quality single crystals, have not provided any definitive proof of the the presence of Dirac states in this material. The conclusion was hampered by the existence of trivial bands at the Fermi level, which significantly contribute to the electrical transport. In particular, CMA effect was not resolved, and transverse MR was found to obey the Kohler's scaling. From the analysis of the Hall effect and the SdH oscillations, very high mobilities of charge carriers with small effective masses were extracted. However, the derived Berry phases, different from the value of π expected for Dirac fermions, indicate that the SdH effect is governed predominantly by trivial electronic states. This finding is in concert with the electronic band structure calculations, which showed that the Dirac point in $PtTe_2$ is located below the Fermi level[3]. Further investigations performed on suitably doped or pressurized material might result in observation of clear contribution of Dirac states to its transport properties, caused by appropriate tuning the chemical potential. Based on the hitherto obtained results, $PtTe_2$ can be classified as a semimetal with moderate degree of the charge carriers compensation.

Methods

Single crystals of $PtTe_2$ were grown by flux method. High-purity constituents (Pt 5 N, Te 6 N), taken in atomic ratio 1:20, were placed in an alumina crucible covered by molybdenum foil strainer and capped with another inverted alumina crucible. This set was sealed inside a quartz tube under partial Ar gas atmosphere. The ampoule tube was heated up to 1150 °C, held at this temperature for 24 hours, then quickly cooled down to 850 °C at a rate of 50 °C/h, kept at this temperature for 360 hours, followed by slow cooling down to 550 °C at a rate of 5 °C/h. Subsequently, the tube was quenched in cold water. Upon flux removal by centrifugation, multitude of single crystals with typical dimensions $3 \times 2 \times 0.4\,mm^3$ were isolated. Their had metallic luster and were found stable against air and moisture.

Chemical composition of the single crystals obtained was checked by energy-dispersive X-ray analysis using a FEI scanning electron microscope equipped with an EDAX Genesis XM4 spectrometer. The average elemental ratio Pt: Te = 35.2(5): 64.8(3) was derived, in accord with the expected stoichiometry. The crystal structure of the single crystals was examined by X-ray diffraction on a KUMA Diffraction KM-4 four-circle diffractometer equipped with a CCD camera, using graphite-monochromatized Cu-Kα1 radiation. The hexagonal CdI_2-type crystal structure (space group $P\bar{3}m1$, Wyckoff No. 164) reported in ref.[62] was confirmed, with the lattice parameters very close to the literature values.

Crystallinity and orientation of the crystal used in the electrical transport studies was checked by Laue backscattering technique employing a Proto LAUE-COS system. Due to the layered crystal structure of $PtTe_2$ it was possible to obtain very thin samples by scotch-tape technique with their surface corresponding to the $a - b$ plane of the hexagonal unit cell of the compound. Rectangular-shaped specimen with dimensions $2.9 \times 1.3 \times 0.04\,mm^3$ was cut from the cleaved single crystal using a scalpel. Electrical contacts were made from 50 μm thick silver wires attached to the sample using silver epoxy paste. Electrical transport measurements were carried out within the temperature range 2–300 K and in magnetic field up to 9 μT using a conventional four-point ac technique implemented in a Quantum Design PPMS platform.

Data availability. The datasets analysed during the current study are available from the corresponding author on reasonable request.

References

1. Hasan, M. Z., Xu, S.-Y., Belopolski, I. & Huang, S.-M. Discovery of Weyl fermion semimetals and topological Fermi arc states. *Ann. Rev. Cond. Mat. Phys.* **8**, 289–309 (2017).
2. Armitage, N. P., Mele, E. J. & Vishwanath, A. Weyl and Dirac semimetals in three dimensional solids. *Rev. Mod. Phys.* **90**, 015001 (2017).

3. Yan, M. *et al*. Lorentz-violating type-II Dirac fermions in transition metal dichalcogenide $PtTe_2$. *Nat. Commun.* **8**, 257 (2017).
4. Soluyanov, A. A. *et al*. Type-II Weyl semimetals. *Nature* **527**, 495–498 (2015).
5. Yang, B.-J. & Nagaosa, N. Classification of stable three-dimensional Dirac semimetals with nontrivial topology. *Nat. Commun.* **5**, 4898 (2014).
6. Nielsen, H. B. & Ninomiya, M. The Adler-Bell-Jackiw anomaly and Weyl fermions in a crystal. *Phys. Lett. B* **130**, 389–396 (1983).
7. Li, C. Z. *et al*. Giant negative magnetoresistance induced by the chiral anomaly in individual Cd_3As_2 nanowires. *Nature Commun.* **6**, 10137 (2015).
8. Li, Q. *et al*. Chiral magnetic effect in $ZrTe_5$. *Nat. Phys.* **12**, 550 (2016).
9. Hirschberger, M. *et al*. The chiral anomaly and thermopower of Weyl fermions in the half-Heusler GdPtBi. *Nat. Mater.* **15**, 1161 (2016).
10. Niemann, A. C. *et al*. Chiral magnetoresistance in the Weyl semimetal NbP. *Sci. Rep.* **7**, 43394 (2017).
11. Xiong, J. *et al*. Evidence for the chiral anomaly in the Dirac semimetal Na_3Bi. *Science* **350**, 413 (2015).
12. Lv, Y.-Y. *et al*. Experimental observation of anisotropic Adler-Bell-Jackiw anomaly in type-II Weyl semimetal $WTe_{1.98}$ crystals at the quasiclassical regime. *Phys. Rev. Lett.* **118**, 096603 (2017).
13. Wang, L.-X., Li, C.-Z., Yu, D.-P. & Liao, Z.-M. Aharonov–Bohm oscillations in Dirac semimetal Cd_3As_2 nanowires. *Nat. Commun.* **7**, 10769 (2016).
14. Deng, K. *et al*. Experimental observation of topological Fermi arcs in type-II Weyl semimetal $MoTe_2$. *Nat. Phys.* **12**, 1105–1110 (2016).
15. Li, P. *et al*. Evidence for topological type-II Weyl semimetal WTe_2. *Nat. Commun.* **8**, 2150 (2017).
16. Lv, B. Q. *et al*. Experimental discovery of weyl semimetal TaAs. *Phys. Rev. X* **5**, 031013 (2015).
17. Chang, T.-R. *et al*. Type-II symmetry-protected topological Dirac semimetals. *Phys. Rev. Lett.* **119**, 026404 (2017).
18. Zhang, K. *et al*. Experimental evidence for type-II Dirac semimetal in $PtSe_2$. *Phys. Rev. B* **96**, 125102 (2017).
19. Autès, G., Gresch, D., Troyer, M., Soluyanov, A. A. & Yazyev, O. V. Robust type-II Weyl semimetal phase in transition metal diphosphides *XP* ($X =$ Mo, W). *Phys. Rev. Lett.* **117**, 066402 (2016).
20. Huang, H., Zhou, S. & Duan, W. Type-II Dirac fermions in the $PtSe_2$ class of transition metal dichalcogenides. *Phys. Rev. B* **94**, 121117 (2016).
21. Bruno, F. Y. *et al*. Observation of large topologically trivial Fermi arcs in the candidate type-II Weyl semimetal WTe_2. *Phys. Rev. B* **94**, 121112 (2016).
22. Noh, H.-J. *et al*. Experimental realization of type-II Dirac fermions in a $PdTe_2$ Superconductor. *Phys. Rev. Lett.* **119**, 016401 (2017).
23. Wang, Y. *et al*. De Hass-van Alphen and magnetoresistance reveal predominantly single-band transport behavior in $PdTe_2$. *Sci. Rep.* **6**, 31554 (2016).
24. Fei, F. *et al*. Nontrivial Berry phase and type-II Dirac transport in the layered material $PdTe_2$. *Phys. Rev. B* **96**, 041201 (2017).
25. Sun, S., Wang, Q., Guo, P.-J., Liu, K. & Lei, H. Large magnetoresistance in LaBi: Origin of field-induced resistivity upturn and plateau in compensated semimetals. *New J. Phys.* **18**, 082002 (2016).
26. Pavlosiuk, O., Kleinert, M., Swatek, P., Kaczorowski, D. & Wiśniewski, P. Fermi surface topology and magnetotransport in semimetallic LuSb. *Sci. Rep.* **7**, 12822 (2017).
27. Pavlosiuk, O., Swatek, P., Kaczorowski, D. & Wiśniewski, P. Magnetoresistance in LuBi and YBi semimetals due to nearly perfect carrier compensation. *Phys. Rev. B* **97**, 235132 (2018).
28. Shekhar, C. *et al*. Extremely large magnetoresistance and ultrahigh mobility in the topological Weyl semimetal candidate NbP. *Nat. Phys.* **11**, 645 (2015).
29. Li, Y. *et al*. Resistivity plateau and negative magnetoresistance in the topological semimetal $TaSb_2$. *Phys. Rev. B* **94**, 121115 (2016).
30. Singha, R., Pariari, A. K., Satpati, B. & Mandal, P. Large nonsaturating magnetoresistance and signature of nondegenerate Dirac nodes in ZrSiS. *Proc. Natl. Acad. Sci.* **114**, 2468 (2017).
31. Hosen, M. M. *et al*. Tunability of the topological nodal-line semimetal phase in ZrSi*X*-type materials ($X =$ S, Se, Te). *Phys. Rev. B* **95**, 161101 (2017).
32. Zhao, Y. *et al*. Anisotropic magnetotransport and exotic longitudinal linear magnetoresistance in WTe_2 crystals. *Phys. Rev. B* **92**, 041104 (2015).
33. Du, X., Tsai, S.-W., Maslov, D. L. & Hebard, A. F. Metal-insulator-like behavior in semimetallic bismuth and graphite. *Phys. Rev. Lett.* **94**, 166601 (2005).
34. Wang, Y. L. *et al*. Origin of the turn-on temperature behavior in WTe_2. *Phys. Rev. B* **92**, 180402 (2015).
35. Zeng, L.-K. *et al*. Compensated semimetal LaSb with unsaturated magnetoresistance. *Phys. Rev. Lett.* **117**, 127204 (2016).
36. Niu, X. H. *et al*. Presence of exotic electronic surface states in LaBi and LaSb. *Phys. Rev. B* **94**, 165163 (2016).
37. Pavlosiuk, O., Swatek, P. & Wiśniewski, P. Giant magnetoresistance, three-dimensional Fermi surface and origin of resistivity plateau in YSb semimetal. *Sci. Rep.* **6**, 38691 (2016).
38. Kumar, N. *et al*. Observation of pseudo-two-dimensional electron transport in the rock salt-type topological semimetal LaBi. *Phys. Rev. B* **93**, 241106 (2016).
39. Ghimire, N. J., Botana, A. S., Phelan, D., Zheng, H. & Mitchell, J. F. Magnetotransport of single crystalline YSb. *J. Phys. Condens. Matter* **28**, 235601 (2016).
40. Han, F. *et al*. Separation of electron and hole dynamics in the semimetal LaSb. *Phys. Rev. B* **96**, 125112 (2017).
41. Xu, J. *et al*. Origin of the extremely large magnetoresistance in the semimetal YSb. *Phys. Rev. B* **96**, 075159 (2017).
42. Chen, F. C. *et al*. Extremely large magnetoresistance in the type-II Weyl semimetal $MoTe_2$. *Phys. Rev. B* **94**, 235154 (2016).
43. Kumar, N. *et al*. Extremely high magnetoresistance and conductivity in the type-II Weyl semimetals WP_2 and MoP_2. *Nat. Commun.* **8**, 1642 (2017).
44. Wang, X. *et al*. Evidence of both surface and bulk Dirac bands and anisotropic nonsaturating magnetoresistance in ZrSiS. *Adv. Electr. Mater.* **2**, 1600228 (2016).
45. Ziman, J. *Principles of the Theory of Solids* (Cambridge University Press, 1972).
46. Shoenberg, D. *Magnetic Oscillations in Metals* (Cambridge University Press, 1984).
47. Ando, Y. Topological insulator materials. *J. Phys. Soc. Jpn.* **82**, 102001 (2013).
48. Wang, C. M., Lu, H. Z. & Shen, S. Q. Anomalous phase shift of quantum oscillations in 3D topological semimetals. *Phys. Rev. Lett.* **117**, 077201 (2016).
49. Li, C. *et al*. Rules for phase shifts of quantum oscillations in topological nodal-line semimetals. *Phys. Rev. Lett.* **120**, 146602 (2018).
50. Taskin, A. A. & Ando, Y. Berry phase of nonideal Dirac fermions in topological insulators. *Phys. Rev. B* **84**, 035301 (2011).
51. Hu, J. *et al*. π Berry phase and Zeeman splitting of Weyl semimetal TaP. *Sci. Rep.* **6**, 18674 (2016).
52. Gao, W. *et al*. Extremely large magnetoresistance in a topological semimetal candidate pyrite $PtBi_2$. *Phys. Rev. Lett.* **118**, 256601 (2017).
53. Wang, A. *et al*. Large magnetoresistance in the type-II Weyl semimetal WP_2. *Phys. Rev. B* **96**, 121107 (2017).
54. Liang, T. *et al*. Ultrahigh mobility and giant magnetoresistance in the Dirac semimetal Cd_3As_2. *Nat. Mater.* **14**, 280–284 (2015).
55. Luo, Y. *et al*. Hall effect in the extremely large magnetoresistance semimetal WTe_2. *Appl. Phys. Lett.* **107**, 182411 (2015).
56. Hu, J. *et al*. Nearly massless Dirac fermions and strong Zeeman splitting in the nodal-line semimetal ZrSiS probed by de Haas - van Alphen quantum oscillations. *Phys. Rev. B* **96**, 045127 (2017).
57. Pippard, A. *Magnetoresistance in Metals* (Cambridge University Press, 2009).

58. Miller, D. & Laikhtman, B. Longitudinal magnetoresistance of superlattices caused by barrier inhomogeneity. *Phys. Rev. B* **54**, 10669 (1996).
59. Argyres, P. N. & Adams, E. N. Longitudinal magnetoresistance in the quantum limit. *Phys. Rev.* **104**, 900 (1956).
60. Stroud, D. & Pan, F. P. Effect of isolated inhomogeneities on the galvanomagnetic properties of solids. *Phys. Rev. B* **13**, 1434 (1976).
61. Pal, H. K. & Maslov, D. L. Necessary and sufficient condition for longitudinal magnetoresistance. *Phys. Rev. B* **81**, 214438 (2010).
62. Faruseth, S., Selte, K. & Kjekshus, A. Redetermined crystal structures of $NiTe_2$, $PdTe_2$, PtS_2, $PtSe_2$ and $PtTe_2$. *Acta Chem. Scand.* **19**, 257 (1965).

Author Contributions

D.K. conceived the experiments and performed preliminary electrical transport studies. O.P. conducted the experiments and analysed the data. Both authors contributed to discussion of the results and writing the manuscript.

Additional Information

Competing Interests: The authors declare no competing interests.

Publisher's note: Springer Nature remains neutral with regard to jurisdictional claims in published maps and institutional affiliations.

Open Access This article is licensed under a Creative Commons Attribution 4.0 International License, which permits use, sharing, adaptation, distribution and reproduction in any medium or format, as long as you give appropriate credit to the original author(s) and the source, provide a link to the Creative Commons license, and indicate if changes were made. The images or other third party material in this article are included in the article's Creative Commons license, unless indicated otherwise in a credit line to the material. If material is not included in the article's Creative Commons license and your intended use is not permitted by statutory regulation or exceeds the permitted use, you will need to obtain permission directly from the copyright holder. To view a copy of this license, visit http://creativecommons.org/licenses/by/4.0/.

© The Author(s) 2018